

Low frequency variability of Southern Ocean jets

Andrew F. Thompson^{1,2} and Kelvin J. Richards³

Received 26 October 2010; revised 11 June 2011; accepted 23 June 2011; published 20 September 2011.

[1] Both observations and high resolution numerical models show that the Southern Ocean circumpolar flow is concentrated in a large number (approximately 8 to 12) of narrow filamentary jets. It is shown here that coherent jets exhibit a range of low frequency variability, on timescales of months to years, that can lead to displacement and to intermittent formation and dissipation of jets. Using output from an eddy-resolving ocean general circulation model in local regions near topographic features, the impact of energy exchange between eddy and mean flow components on jet persistence and variability is examined. A novel approach that uses a time-dependent definition of the mean flow provides a clearer picture of eddy-mean flow interactions in regions with spatially and temporally varying flow structure. The dynamics are largely consistent with those in idealized quasi-geostrophic models, including topographically-organized and surface-enhanced Reynolds stress forcing of the mean flow. Jets form during periods of enhanced eddy activity, but may persist long after the eddy activity has decayed. Similarly, jets may evolve in a downstream sense, with jet formation localized near topography and undergoing modification in response to changing bathymetry. The evolution of both temperature and potential vorticity is used to show that the low-frequency variability of the jets impacts water mass structure and tracer transport. This study highlights various examples of Southern Ocean dynamics that will prove difficult to capture through parameterizations in coarser climate models.

Citation: Thompson, A. F., and K. J. Richards (2011), Low frequency variability of Southern Ocean jets, *J. Geophys. Res.*, 116, C09022, doi:10.1029/2010JC006749.

1. Introduction

[2] The circulation of the Southern Ocean differs significantly from basin circulations in the Atlantic, Pacific and Indian Oceans. The geography of the southern hemisphere permits a strong circumpolar flow, the Antarctic Circumpolar Current (ACC), which has many similarities with zonally-symmetric flows in planetary atmospheres [Rintoul *et al.*, 2001; Williams *et al.*, 2007; Thompson, 2008]. One of the most striking aspects of the circulation in large planetary atmospheres, as well as the Southern Ocean, is the organization of the flow into strong narrow bands known as jets. Jets impact the transport and dispersion of heat, chemicals and, in the ocean, biomass [Kamenkovich *et al.*, 2009; Marshall *et al.*, 2006]. Jets typically act as barriers to (cross-jet) transport [Marshall *et al.*, 2006], but few jets are absolute barriers and have been termed “leaky” [Esler, 2008; Naveira-Garabato *et al.*, 2011] when weak trans-

port occurs. Baroclinic jets also tend to be sites of eddy generation and thus may, in certain locations, enhance mixing [Bower *et al.*, 1985]. Theories relating transport to local mean flow strength and eddy kinetic energy levels [e.g., Ferrari and Nikurashin, 2010] are still being explored.

[3] Important differences exist between oceanic and atmospheric jets. The difference in scale of the first baroclinic deformation radius causes the horizontal length scale of ocean jets to be considerably smaller than their atmospheric counterparts. This permits a more complex and intricate structure in the ocean [e.g., Hallberg and Gnanadesikan, 2006; Sokolov and Rintoul, 2007]. Furthermore, the Southern Ocean is particularly sensitive to topographic features that provide the primary source of momentum dissipation through topographic form stress [Munk and Palmén, 1951; Olbers *et al.*, 2004]. Topography also induces flow instability and generates internal waves that can enhance diabatic processes through breaking. A unifying feature of atmospheric and oceanic jets is that jet persistence, or lack thereof, is governed largely by the interaction of the mean flow with eddying motion [Hughes and Ash, 2001].

[4] Traditionally, fronts in the ACC have been identified using water mass properties based on analysis of latitude-depth sections of temperature and salinity [Orsi *et al.*, 1995; Belkin and Gordon, 1996]. This approach led to a view of the ACC being composed of three or four quasi-steady, circumpolar fronts. In the last decade, a more dynamic picture

¹British Antarctic Survey, Cambridge, UK.

²Now at Division of Geological and Planetary Sciences, California Institute of Technology, Pasadena, California, USA.

³International Pacific Research Center, School of Ocean and Earth Science and Technology, University of Hawaii at Manoa, Honolulu, Hawaii, USA.

of the ACC has developed. As opposed to a small number of circumpolar, steady fronts, the ACC is now seen as being comprised of an intricate web of rivulet jets, with jets typically identified by velocity extrema (or gradients in sea surface height) rather than water mass gradients. This alternative picture of the ACC has principally arisen from analysis of satellite altimetry data, most notably *Hughes and Ash* [2001] and *Sokolov and Rintoul* [2007, 2009] as well as eddy-resolving ocean general circulation models [*Hallberg and Gnanadesikan*, 2006]. The major features of the fine frontal structure of the ACC are:

[5] 1. Rivulet jets have a narrower spacing than traditional hydrographic fronts. *Sokolov and Rintoul* [2007, 2009] suggest that ten to twelve distinct fronts or jets may be crossed in a meridional section spanning the ACC. A characteristic length scale describing the *local* jet spacing is generally evident, (e.g., *Sinha and Richards*' [1999] calculation of a Rhines scale), however the jet spacing is not uniform across the ACC. In certain cases, jets may be separated by as little as 1 degree of latitude.

[6] 2. *Sokolov and Rintoul* [2002] suggest multiple jets represent branches of the primary fronts. However, these branches are observed to spontaneously form and dissipate, merge and split, and migrate to different latitudes. Small-scale jets are difficult to track circumpolarly, although they are often consistently located at particular sites due to the influence of topographic features [*Thompson et al.*, 2010; *Lu and Speer*, 2010].

[7] 3. The role of eddies in sustaining or sharpening jets may vary along the path of the ACC. In zonally-symmetric domains, horizontal mixing by eddies typically acts to enhance the mean flow through convergence of eastward momentum. Within the Southern Ocean, however, eddies are observed to both enhance and dissipate jets [*Hughes and Ash*, 2001; *Wilson and Williams*, 2006]. In fact, *Williams et al.* [2007] have suggested that eddies have life cycles that describe the process of jet formation and growth followed by jet decay along the path of the ACC, similar to storm tracks in the atmosphere.

[8] Despite improvements in Southern Ocean observational and modeling capabilities, the dynamics, e.g. eddy-mean flow interactions, that relate the formation of small-scale jets to long-term water mass boundaries remain unclear. Many of the jet characteristics described above have now been verified in eddy-resolving ocean general circulation models (OGCMs) (see the review by *Ivchenko et al.* [2008]), although all OGCMs have shown that increasing spatial resolution leads to more intricate jet structure. The high spatial and temporal resolution of OGCMs, along with broad horizontal and vertical coverage, is crucial as it has become increasingly apparent that a complete description of jet behavior in the ACC must account for local inhomogeneities, of which topographic features make a major contribution.

[9] While the present study falls short of a comprehensive description of jet dynamics, it does address dynamical mechanisms that give rise to unsteady jet behavior in the Southern Ocean as well as the impact this variability has on water mass structure (measured here by changes in temperature and potential vorticity distributions). A specific focus is the importance of topography in inducing the low frequency variability. Examples of topographically-induced

jet variability have been explored in the context of two- and three-layer quasi-geostrophic (QG) simulations [*Hogg and Blundell*, 2006; *Thompson*, 2010]. However, many of the assumptions required in the QG formulation are invalid in the Southern Ocean; in particular, the height of topographic features is often the same order of magnitude as the ocean depth. The primitive equation model used here includes a more realistic representation of the bathymetry and remains valid for both tall and steep obstacles. Thus a key aim of this study is to determine whether the dynamics observed in the QG simulations remain active in the more realistic flows.

[10] A brief review of topography-jet interactions found in QG models is provided in section 2. Details of the numerical model and the diagnostics used in this study are given in section 3. Section 4 describes the jet-topography interactions active in these realistic flows and in section 5 the implications of jet variability on mixing is considered by analyzing time series of temperature and isopycnal potential vorticity. A summary and discussion follow in section 6.

2. Jets and Topography: Eddy-Mean Flow Interactions

[11] The most basic ingredient for jet formation is a large-scale gradient of potential vorticity (PV) that supports Rossby waves and produces a preference for flow perpendicular to the gradient through PV conservation. In the ocean topographic slopes make a significant and often dominant contribution to the PV gradients, especially in the ACC, such that topography can act to steer the mean flow [*Marshall*, 1995]. Topographic steering can impact stability characteristics and feed back on eddy-mean flow interactions [*Spall*, 2000], which may in turn modify the effectiveness of the mean flow, or jet, as a transport barrier. In this section we briefly review two mechanisms by which topography influences jet structure and transport; *Thompson* [2010] provides further details.

2.1. Drifting Jets

[12] Jet formation and persistence in stratified flows can be described as a balance between eddy generation through baroclinic instability and a convergence of eastward momentum at the jet cores that results from eddy-induced PV mixing on the jet flanks [*Panetta*, 1993; *Lee*, 1997; *Vallis*, 2006]. The convergence of eastward momentum arises through a transfer between eddy kinetic energy (EKE) and mean kinetic energy (MKE) components due to Reynolds stress correlations (see section 3). When topography contributes to the PV gradient, the magnitude and orientation of the PV gradient will vary spatially. Under certain conditions, specifically if the length scale of the topography is comparable to the length scale of the jet spacing, the jet may experience an asymmetry in mean-flow forcing by Reynolds stresses (*Thompson* [2010] illustrates a simple example with a zonal ridge). In QG simulations this asymmetry leads to a meridional drift of the jet core across the mean PV gradient with jets moving toward regions of weaker PV gradient. The displaced jet decays as it enters a weak PV gradient region, and a new jets forms in the vacated region. This process and the sense of the drift is described schematically in Figure 1 left.

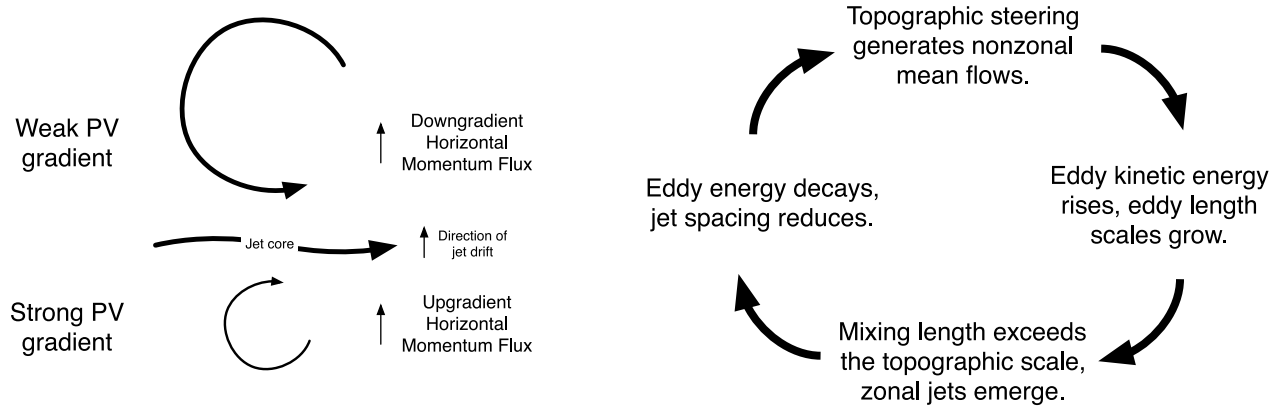


Figure 1. (left) Schematic showing how local topographic modifications to the potential vorticity (PV) gradient can produce asymmetric jet forcing that leads to jet drift across the mean PV gradient as described in section 2.1. (right) Schematic of oscillatory jet behavior arising from interaction between topography and a baroclinically unstable flow as described in section 2.2.

2.2. Steered-Zonal Oscillations

[13] Topographic steering, through alteration of the strength and orientation of the mean flow, may also feed back on eddy generation through baroclinic instability. Arbitrarily weak meridional shear is susceptible to linear instability [Pedlosky, 1987; Walker and Pedlosky, 2002], and equilibrated eddy energy levels can be 100 to 1000 times larger in baroclinic turbulence generated by a mean flow with a meridional component [Arbic and Flierl, 2004; Smith, 2007]. Since jet spacing is related to EKE levels through the Rhines scale,

$$\ell_R \sim \sqrt{U_e/\beta}, \quad (1)$$

where U_e is an eddy velocity and β is the barotropic large-scale PV gradient (see Sinha and Richards [1999] for application in a Southern Ocean model), topography may also impact flow structure beyond simple steering arguments.

[14] When the Rhines scale and the topographic scale are comparable, a flow regime can develop that is characterized by continuous oscillations between topographically-steered and zonally-symmetric states [Hogg and Blundell, 2006; Thompson, 2010]. The transition between these states is accompanied by a complete reorganization of the jet structure. The process that leads to these oscillations is described in the schematic in Figure 1 right. The critical behavior is the enhanced generation of EKE in the topographically-steered flow state due to meridional deflection of the mean flow. As the stronger eddies mix over the local signature of the topography, steering is reduced. In this “zonal” state, the energy of the system decays until steering becomes important again.

3. OFES Model and Diagnostics

[15] To explore the interaction between jets and topography in a more realistic context, we examine output from the Ocean General Circulation Model for the Earth Simulator (OFES). OFES is based on the Modular Ocean Model version 3 (MOM3) developed at GFDL, while parallelization for the Earth Simulator allows decadal integrations of the

global ocean circulation in an eddying regime [Masumoto *et al.*, 2004]. OFES has a horizontal resolution of 0.1 degree and has 54 vertical layers of variable depth. The magnitude and scales of variability of the velocity and sea surface height gradient fields in OFES are consistent with those shown in other high resolution ocean models [Hallberg and Gnanadesikan, 2006; McClean *et al.*, 2008; Mazloff *et al.*, 2010] as well as altimetry data [Sokolov and Rintoul, 2007]. As the model solves a dynamically consistent set of equations relevant to the Southern Ocean, we regard the model as a useful surrogate for the real ocean. Besides improving on the horizontal resolution available from satellite data, output from OFES also allows examination of the vertical jet structure, which is a fundamental limitation of altimetry. Analysis covers a period of 8 years from 1990 through 1997 following a 50 year spin up with climatological forcing. We focus on the Indian and Pacific sectors of the ACC shown in Figure 2. Our analysis is confined to a set of local regions that include a variety of topographic features.

[16] Figure 3 shows a snapshot of speed ($\sqrt{u^2 + v^2}$) from the OFES model at a depth of 250 m. The white boxes indicate regions that are discussed in greater detail in the following section; the zonally-averaged topography for each box is given in Figure 3 (bottom). A key aspect of this study is the identification of eddy-mean flow interactions that lead to low frequency variations in coherent jets. These interactions vary both spatially and temporally, and averaging over too large a space or timescale will smooth out details of the dynamics. In order to capture the low frequency variations, the temporal “mean” flow $\bar{\mathbf{u}}(\mathbf{x}, t)$ is determined by taking the Fourier transform of the velocity time series and discarding contributions from frequencies greater than $\omega_{\text{cut}} = 0.070 \approx 2\pi/90 \text{ days}^{-1}$. The eddy velocities are then defined by $\mathbf{u}'(\mathbf{x}, t) = \mathbf{u} - \bar{\mathbf{u}}$. Sensitivity studies have shown that the results in section 4 are not qualitatively dependent on the choice of ω_{cut} if the corresponding period $T_{\text{cut}} = 2\pi/\omega_{\text{cut}}$ is between two and six months.

[17] Following previous work on eddy-mean flow interactions in the ACC [Hughes and Ash, 2001; Williams *et al.*, 2007; Lenn *et al.*, 2011], we consider the role of Reynolds stresses on setting jet structure. The focus here is on the

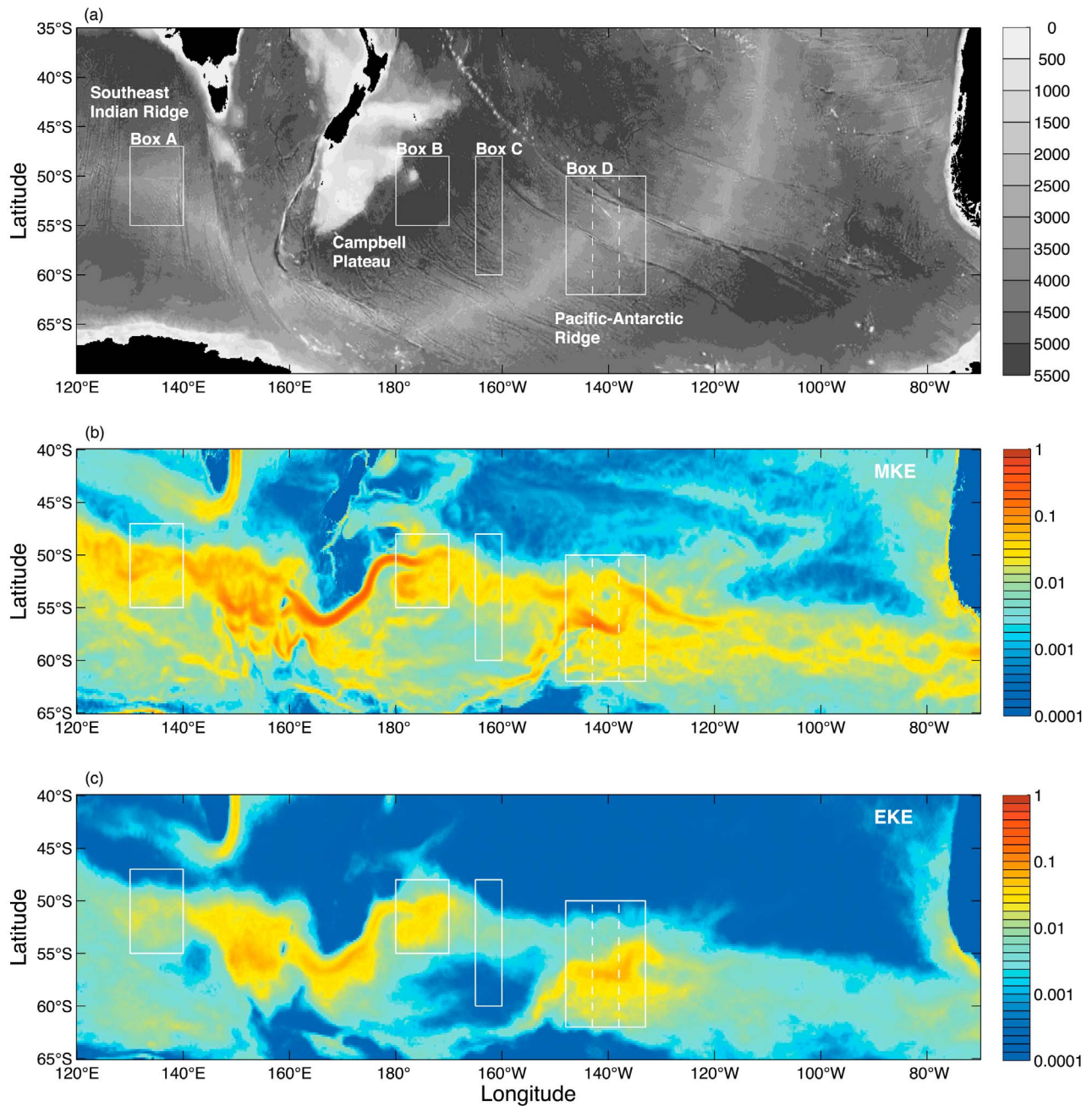


Figure 2. (a) Bathymetry of the Indian and Pacific sector of the Southern Ocean. Colors indicate ocean depth in meters; land is colored black. The labeled white boxes refer to domains discussed in section 4. (b) Time-averaged mean kinetic energy ($\text{m}^2 \text{s}^{-2}$) at 250 m depth, calculated from eight years of OFES data (see section 3). Mean velocities are determined by using a low-pass filter with a three month cut-off. (c) Time averaged eddy kinetic energy ($\text{m}^2 \text{s}^{-2}$) calculated from OFES data. Eddy velocities are the difference between the total velocity and mean velocity described above. Land is indicated by gray in Figures 2b and 2c.

transfer of energy between eddy and mean components, which involves the correlation between the mean flow and Reynolds stresses. This diagnostic is selected as it is consistent with the flow's efficient organization of the eddy field into coherent zonal structures and it provides a good example of the advantages of allowing for a temporally varying mean flow. The patterns that develop (i.e. the spatially and temporally varying jet behavior) are typically

consistent with patterns seen in the Reynolds stress forcing of the mean flow.

[18] Our derivation below focuses on the horizontal forces generated from horizontal velocities. A typical approach adopted in studies of atmospheric jets is to consider depth-averaged velocities, in which the vertical component of the momentum flux is zero. Due to the equivalent barotropic structure of the ACC, which is well reproduced in the

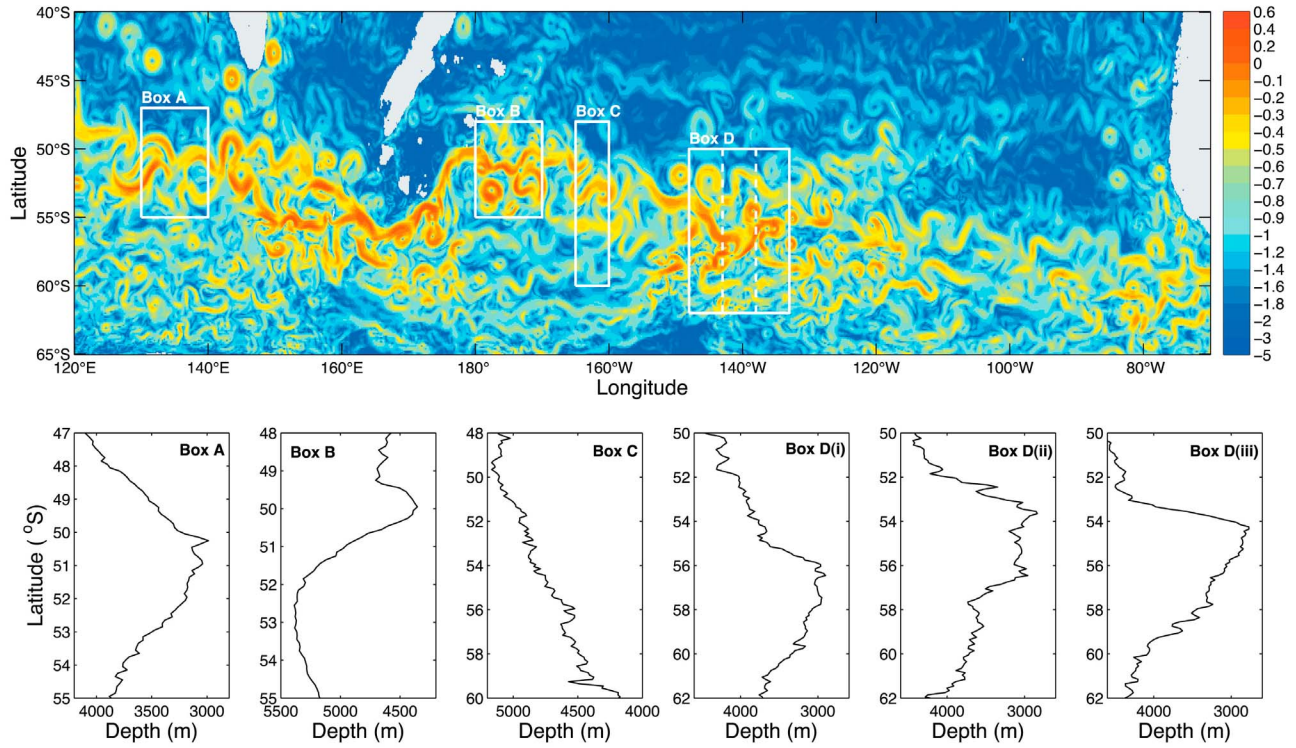


Figure 3. (top) Snapshot of current speed ($\log_{10} \text{ m s}^{-1}$) at 250 m depth from the OFES model. The labeled white boxes refer to domains discussed in section 4. (bottom) The zonally averaged bathymetry (taken from *Smith and Sandwell [1997]*) in these regions. Box D is divided into three sub-boxes each spanning 5 degrees of longitude.

model, the spatial patterns of the eddy-mean flow interactions is largely independent of depth (see further discussion in section 4). Since forcing of the mean flow by Reynolds stresses is surface intensified, we focus primarily on velocities at a depth of 250 m.

[19] For nearly two-dimensional motion ($w \approx 0$), horizontal momentum in the primitive equation model evolves according to

$$\mathbf{u}_t + \mathbf{u} \cdot \nabla \mathbf{u} + f \hat{\mathbf{k}} \times \mathbf{u} = -\frac{\nabla p}{\rho_0} + \mathbf{F}, \quad (2)$$

where \mathbf{u} is the horizontal velocity vector, f is the Coriolis frequency, p is pressure, ρ_0 is a reference density and \mathbf{F} represents frictional terms. Taking a time average over the fast timescale associated with the high frequency variations, indicated by an overbar, (2) becomes

$$\bar{\mathbf{u}}_T + \bar{\mathbf{u}} \cdot \nabla \bar{\mathbf{u}} + f \hat{\mathbf{k}} \times \bar{\mathbf{u}} = -\frac{\nabla \bar{p}}{\rho_0} + \bar{\mathbf{F}} - \overline{\mathbf{u}' \cdot \nabla \mathbf{u}'}, \quad (3)$$

where $\bar{\mathbf{u}}_T$ indicates that the mean flow is evolving on the slow timescale $T > T_{\text{cut}}$. The final term represents the familiar eddy-induced acceleration of the mean flow due to Reynolds stress correlations. Assuming the flow is two-dimensional such that $u'_x + v'_y \approx 0$, the Reynolds stress term can be written as [*Hughes and Ash, 2001*]

$$\mathbf{M} \equiv -\overline{\mathbf{u}' \cdot \nabla \mathbf{u}'} = -\frac{1}{2} \nabla (\overline{u'u'} + \overline{v'v'}) - \hat{\mathbf{k}} \times \overline{\mathbf{u}' \zeta'}, \quad (4)$$

where ζ' is the vertical vorticity component $v'_x - u'_y$ and $\overline{\mathbf{u}' \zeta'}$ is the eddy vorticity flux. A full discussion of this choice of decomposition is provided by *Hughes and Ash [2001]*, but briefly, the first term on the right hand side of (4), the total EKE, may be subsumed in a modified pressure (e.g. a change in sea surface height), while the remaining component

$$\mathbf{N} \equiv -\hat{\mathbf{k}} \times \overline{\mathbf{u}' \zeta'} \quad (5)$$

describes acceleration of the mean flow solely due to eddy fluxes. This decomposition also highlights the relationship between zonal momentum forcing and meridional vorticity fluxes. (The vectors \mathbf{M} and \mathbf{N} are not to be confused with the components of the anisotropic parts of the eddy velocity correlation tensor M, N [*Hoskins et al., 1983*]. We also note that eddy forcing of the mean flow, as described by \mathbf{N} , may be distributed between acceleration of the mean flow and the generation of an ageostrophic circulation through the Coriolis torque term.)

[20] The evolution equations for the mean and eddy energy components are then formed by multiplying (2) by $\bar{\mathbf{u}}$ and \mathbf{u}' respectively and averaging in time. The MKE budget, keeping the notation from above, becomes

$$\frac{\partial}{\partial t} \left(\frac{\bar{\mathbf{u}}^2}{2} \right) = -\nabla \cdot \left(\bar{\mathbf{u}} \frac{\bar{\mathbf{u}}^2}{2} \right) - \nabla \cdot \left[\bar{\mathbf{u}} \left(\frac{\bar{p}}{\rho_0} + \frac{\overline{u'u'}}{2} + \frac{\overline{v'v'}}{2} \right) \right] - \mathcal{F} + \mathcal{R}. \quad (6)$$

Terms on the right hand side represent advection of MKE by the mean flow, work by the mean (modified) pressure flux

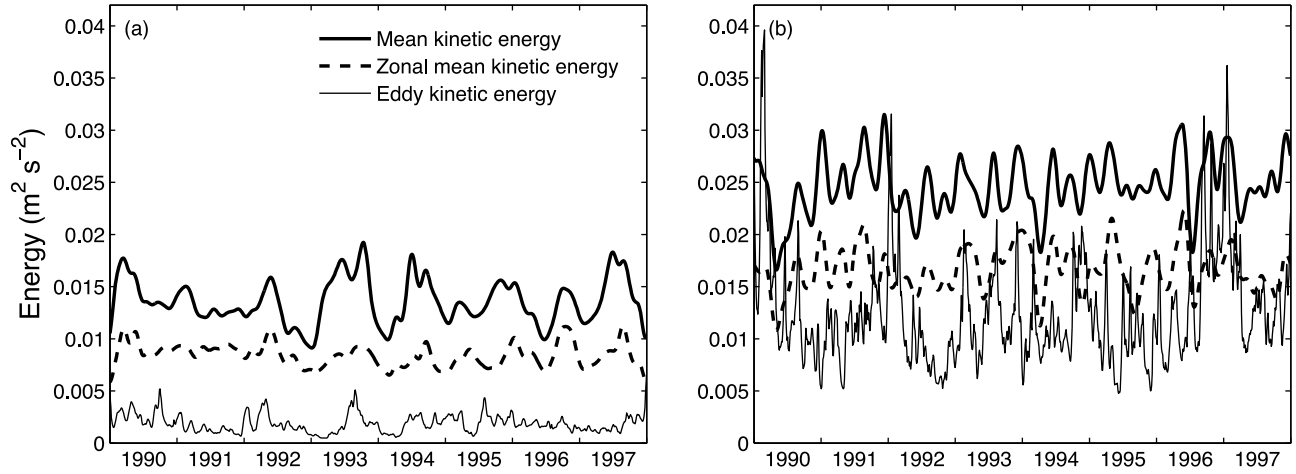


Figure 4. Time series of mean kinetic energy (bold line), the zonal component of mean kinetic energy (dashed line) and eddy kinetic energy (thin line) in two neighboring regions of the Antarctic Circumpolar Current at a depth of 250 m. Definitions of mean and eddy energies are given in section 3. (a) Span of the region 160°W to 155°W and 65°S to 50°S; (b) span of the region 145°W to 140°W and 65°S to 50°S.

(or energy transfer between MKE and potential energy), horizontal and vertical viscous dissipation, \mathcal{F} , and kinetic energy conversion between eddy and mean components,

$$\mathcal{R} = \bar{\mathbf{u}} \cdot \mathbf{N} = [\bar{\mathbf{u}}(\bar{\mathbf{v}'\mathbf{v}'_x} - \bar{\mathbf{v}'\mathbf{u}'_y}) + \bar{\mathbf{v}}(\bar{\mathbf{u}'\mathbf{u}'_y} - \bar{\mathbf{u}'\mathbf{v}'_x})]. \quad (7)$$

Transfer of kinetic energy from eddy to mean components occurs where \mathcal{R} is positive. Note that for a zonally symmetric flow $\bar{\mathbf{v}} = \bar{\mathbf{v}'\mathbf{v}'_x} = 0$, and (7) reduces to the familiar form $\mathcal{R}_{\text{zonal}} = -\bar{\mathbf{u}}(\bar{\mathbf{u}'\mathbf{v}'_y})$. We calculate the full value of \mathcal{R} given in (7), but the quantities shown in section 4 include a further zonal average.

[21] Important insight can also be gained from looking at the eddy forcing of the mean flow. This is most clearly analyzed by considering the divergence of the eddy vorticity flux,

$$\mathcal{Z} \equiv \mathbf{k} \cdot \nabla \times \mathbf{M} = \mathbf{k} \cdot \nabla \times \mathbf{N} = -\nabla \cdot \bar{\mathbf{u}'\boldsymbol{\zeta}'}. \quad (8)$$

This diagnostic removes rotational components and represents a curl applied to the mean momentum [Williams *et al.*, 2007]. The extra derivative in (8) makes it a more challenging quantity to diagnose than \mathcal{R} due to the application of a time-dependent mean flow. We provide a comparison of patterns in \mathcal{R} and \mathcal{Z} in section 4.1.

[22] Diagnosis of the full Eliassen-Palm flux remains beyond the scope of the present paper. It is well known that buoyancy fluxes play a key role in setting the residual overturning across the ACC [Marshall and Radko, 2003]. In fact the PV flux is largely controlled by the buoyancy flux if the eddy length scale is larger than the deformation radius (assuming $\mathbf{v}' \sim b'/N$, where b and N are the buoyancy and buoyancy frequency respectively [Vallis, 2006]). The focus on horizontal momentum fluxes reflects evidence that jets tend to be locally maintained by upgradient momentum fluxes [McIntyre, 1970; Dritschel and McIntyre, 2008; Thompson and Young, 2007]. Documenting the spatial and temporal variability of the ACC's jets is the aim of this study; further questions of how these features impact the

larger-scale overturning would need to consider buoyancy fluxes.

[23] In section 5 we consider the relationship between jet variability and water mass distributions using both temperature and PV. Since PV is conserved along isopycnals in the ocean interior (neglecting diabatic processes), we construct time series of PV on isopycnal surfaces. Data from OFES is provided on 54 levels; PV, q , is first calculated on each level using

$$q = \frac{(f + \zeta)}{\rho_0} \frac{\partial \sigma_2}{\partial z}, \quad (9)$$

where σ_2 is potential density referenced to 2000 m. Once q is calculated at all depths, the values are linearly interpolated onto selected σ_2 surfaces.

4. Southern Ocean Jets in an Eddying OGCM

[24] The ACC exhibits significant longitudinal variability in both flow structure and statistical properties, such as EKE, e.g., Gille [1997] and Figure 2. Figure 4 shows time series of energy levels averaged over 65°S and 50°S and 155–160°W (Figure 4a) and 140–145°W (Figure 4b). EKE is nearly an order of magnitude greater in the downstream region (Figure 4b) and the ratio of EKE to MKE is larger here. The frequency of variability also differs: MKE variability in the upstream region (Figure 4a) is dominated by low frequency modes with periods of a year or longer, while downstream MKE (Figure 4b) has a broader spectral peak with significant contributions from all frequencies nearly down to ω_{cut} . These spatial differences can be attributed largely to the topographic structure in the ACC [Lu and Speer, 2010]. In Figure 4, topography in the upstream region is characterized by a gentle sloping bottom, whereas the downstream region contains sharp bathymetric gradients and transitions associated with the Eltanin and Udintsev Fracture Zones in the Pacific-Antarctic Ridge. Thus, topography influences not only EKE amplitudes, but also

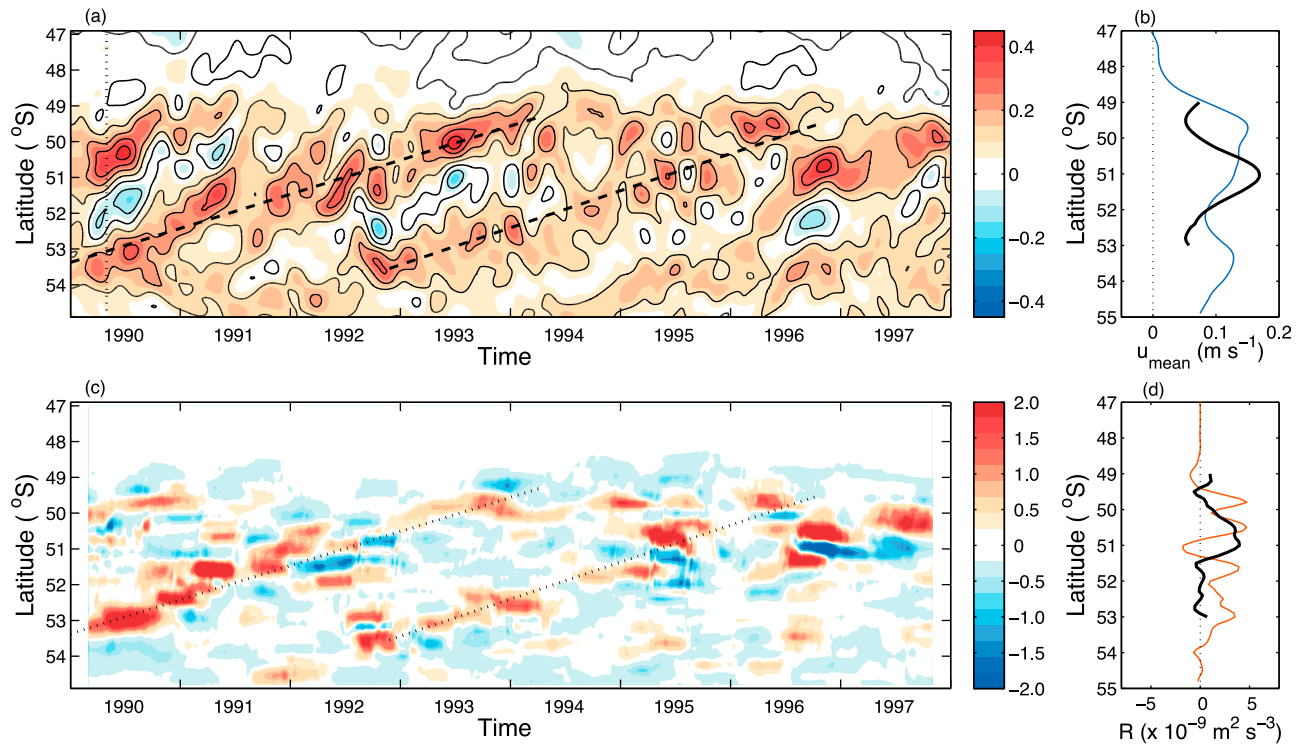


Figure 5. (a) Time-latitude plot of the zonally averaged zonal component of the mean velocity (m s^{-1}) at a depth of 250 m for the region labeled box A in Figure 3: 130°E to 140°E and 55°S to 47°S . The dashed lines indicate the meridional drift of the jet cores with time. A latitude-depth section along the dotted line is shown in Figure 7. (b) Temporally and zonally averaged profile of the zonal component of mean velocity in box A (blue curve) and a time average of this zonal velocity centered on the dashed line and spanning four degrees of latitude (black curve). (c) Time-latitude plot of the zonally averaged \mathcal{R} ($\times 10^{-8} \text{ m}^2 \text{ s}^{-3}$) defined in (7) for the box A region. (d) Time and zonal mean profile of \mathcal{R} (red curve) and a time average along the dotted lines, as above (black curve).

the dominant modes of variability, suggesting that different dynamical processes may be active in different regions.

[25] In this section four regions of the ACC are considered. Region selection is, in part, motivated by comparison with dynamics in the QG simulations (section 2); in particular, the moderately sloped ridge in box A has a length scale comparable to the periodic ridges of Thompson [2010]. These regions do not exhibit a complete set of mechanisms that lead to jet variability in the Southern Ocean, but they do highlight a unifying characteristic of these structures: spatially and temporally localized forcing, often due to topography, followed by a downstream flow evolution. This is evident through the change in flow structure between boxes B and C as well as through the flow transition across box D.

4.1. Box A

[26] Box A covers the region 130°E to 140°E and 55°S to 47°S and is found downstream of Kerguelen Island. The topography of this region is dominated by a single ridge (the Southeast Indian Ridge) with a zonal orientation (Figure 2a). This region is often populated by a number of coherent eddies (Figure 3), but the zonal component of the mean flow is predominant over the meridional component ($\bar{u} \gg \bar{v}$).

[27] Figure 5a shows a time series of the zonally-averaged zonal component of the mean velocity in box A at a depth of 250 m over a period of eight years. The zonal component

of the mean flow is almost always positive (eastward) throughout the time series, except for a few occurrences where westward flow separates two bands of strong eastward flow. Coherent bands, or jets, are evident. Throughout the time series, these jets undergo a slow northward displacement. This displacement, or drift, is not a signature of individual coherent eddies, as the timescale for advection through the domain (roughly a month for a zonal mean velocity of 20 cm s^{-1}) is vastly different from the timescale of the jet evolution.

[28] The region experiences periods with one or two coherent jets with a characteristic spacing of 350 km. As the jets shift northward, new jets tend to form near 54°S . The dashed lines in Figure 5a are linear fits to temperature gradient maxima. Although the velocity drift is coherent and tied to temperature fronts, the jet core is not tied to a particular isotherm (see further discussion in section 5). Thus, labeling these features as a single front is dependent on jet definition. Still, identifying this drift is useful in highlighting eddy-mean flow interactions in the region. For instance, a simple time and zonal average of the zonal velocities in this domain (Figure 5b, blue curve) shows only weak evidence of jet structure. A time and zonal average centered along the dashed lines (Figure 5b, black curve) reveals a clear, nearly-symmetric jet velocity profile.

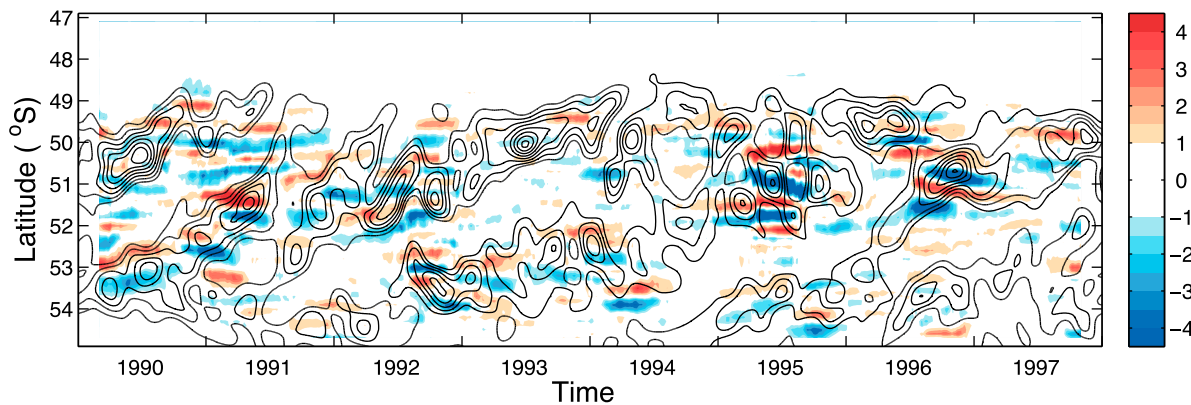


Figure 6. Time-latitude plot of the zonally averaged divergence of the eddy vorticity flux, $-\nabla \cdot \overline{u' \zeta'}$, (8) ($\times 10^{-12} \text{ s}^{-2}$) at a depth of 250 m for the region labeled box A in Figure 3. The contours indicate the zonal component of the mean velocity. Contours are every 0.05 m s^{-1} between 0.1 and 0.5.

[29] The jets in Figure 5a dissipate abruptly north of 49°S near the base of the ridge's northern slope. While the northern (southern) slope nominally enhances (weakens) the background PV gradient, the steepness of the slope means that the topographic contribution to the mean PV gradient is an order of magnitude greater than the planetary PV gradient. Furthermore the Southern Ocean's strong isopycnal tilt provides a strong source of instability nearly uniformly in the core the ACC. Thus the direction of jet drift is likely to be less predictable than in the QG model, where formation preferentially occurs in strong PV gradient regions and drifts into regions of weaker PV gradient. The jets drift at a nearly uniform rate, outside of turbulent fluctuations and meanders, which is consistent with a spatially varying PV gradient that is imposed by topography (i.e. fixed in time). Jets over flat bottomed regions (e.g. eastern Pacific sector) experience more variability, and uniform drift is not observed.

[30] Figure 5c shows the time evolution of the zonally-averaged value \mathcal{R} (7) at 250 m depth; the time series has been smoothed using a two-month running mean. Regions where $\mathcal{R} > 0$ are consistent with a transfer of EKE to MKE. Figure 5c shows that this occurs near the jet cores (dotted lines). The concentration of \mathcal{R} in the jet core is consistent with self-sharpening of the jet structure due to up-gradient momentum fluxes [Dritschel and McIntyre, 2008]. Figure 5d indicates that a simple time and zonal average of \mathcal{R} (red curve) obscures much of the structure apparent in the time series. The black curve, on the other hand, results from a time average centered along the dotted curves in Figure 5c, and reveals the jet structure more clearly. There is evidence of asymmetry in this profile with positive values of \mathcal{R} extending over a larger range of latitude north of the jet core (centered at 51°S). This pattern is consistent with the mean flow being energized preferentially to the north, and is similar to the pattern of energy transfer in the QG simulations with drifting jets. (Note that Thompson [2010] plotted the quantity $\mathcal{R}^* \equiv \overline{u_y(u'v')}$, whereas in the zonally-symmetric case \mathcal{R} (7) reduces to $-\overline{u(u'v')}$. In the former case jet drift tends toward latitudes where $\mathcal{R}^* < 0$, while in the latter case drift tends toward latitudes where $\mathcal{R} > 0$.)

[31] A striking feature of Figure 5c is that despite temporal smoothing, energy transfer between eddy and mean components occurs in bursts localized in both time and

space. Thus the forcing of the jet arises as a series of steps that displace the jet northward through the domain. These punctuated shifts in position, as opposed to a smooth drift, are due to low frequency variations in EKE: strong eddies are efficient at mixing the fluid and accelerating the mean flow. These features are, to a certain extent, tied to topographic features. For example, strong Reynolds stress correlations occur during times of jet formation near 54°S at the base of the ridge.

[32] Figure 6 shows the temporally evolving behavior of the divergence of the eddy vorticity flux \mathcal{Z} (8) with an additional zonal average over box A. Williams *et al.* [2007] analyzed this quantity using time averaged surface properties of the ACC and found an intricate pattern of dipoles and tripoles. Dipoles with positive forcing to the north and negative forcing to the south correspond to eastward acceleration of the mean flow by eddies, while westward acceleration is consistent with the reversed configuration. Williams *et al.* [2007] also suggest that tripoles correspond to a transfer of momentum from the core to the flanks of the jets. Figure 6 again emphasizes that the location of eddy forcing shifts slowly through the domain over the eight year period, indicating that a suitable time average provides a clearer picture of eddy-mean flow interactions. The eddy forcing here is also comprised of dipoles and tripoles with dipoles corresponding to eastward acceleration occurring predominantly in the southern portion of the domain where the jets are initiated. A number of tripolar patterns are also apparent along the jet cores; these structures provide a mechanism for transferring zonal momentum meridionally across the domain. Figure 6 also shows that eddy forcing of the mean flow occurs through discrete events as discussed above.

[33] Figure 7 shows three latitude-depth plots where the zonal component of the mean flow (contours) is plotted along with an eddy forcing term (color). In Figure 7a the zonal mean of \mathcal{Z} (divergence of the eddy vorticity flux) is plotted along with the zonal mean flow at a time when the jets undergo an equatorward drift (dotted line in early 1990 in Figure 5a). The values are averaged over the zonal extent of box A. In both jets \mathcal{Z} is negative in the jet core and positive on the flanks, which is consistent with an eastward acceleration on the northern flank and a westward acceleration

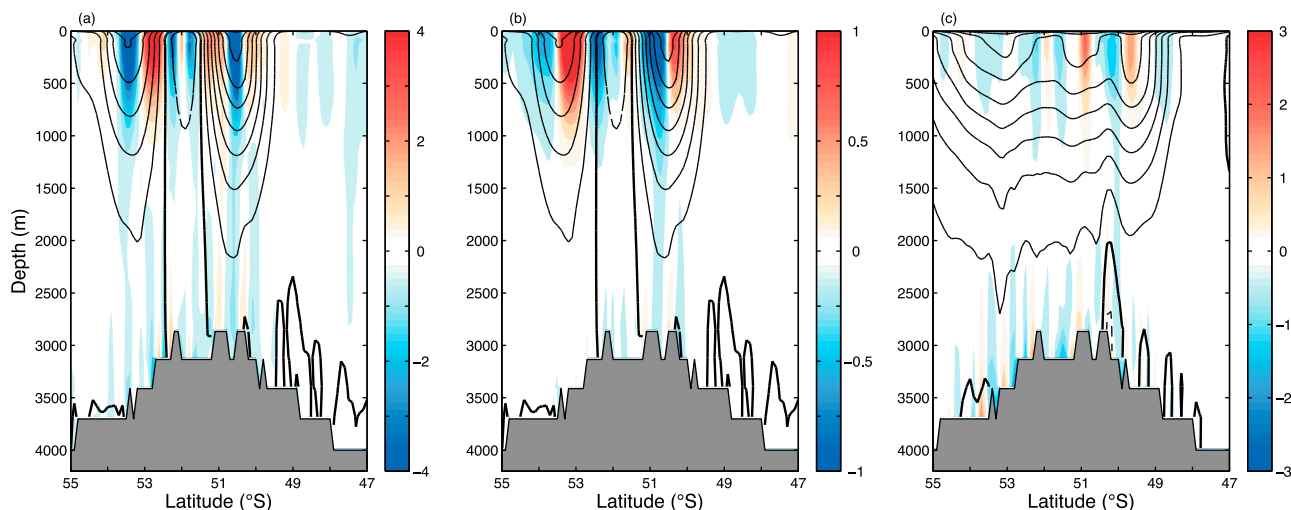


Figure 7. Vertical profiles of the zonally averaged zonal component of mean velocity (contours) and (a, c) the zonal average of Z (color, units of $\times 10^{-12} \text{ s}^{-2}$) (8) and (b) the zonally averaged zonal component of the eddy momentum forcing $N_x \approx -(\overline{u'v'})_y$ (color, units of $\times 10^{-7} \text{ m s}^{-2}$) (5). The values are averaged zonally across box A (Figure 3) and over a period of three months centered at the time corresponding to the dotted curve in Figure 5a (Figures 7a and 7b) and over the two year period 1990 to 1991 (Figure 7c). Contour intervals are 0.05 m s^{-1} in Figures 7a and 7b and 0.02 m s^{-1} in Figure 7c.

ation on the southern flank, which would displace the mean flow to the north. The pattern of Reynolds stresses (the color shows the zonal average of N_x , which has the same structure and magnitude as $\approx -(\overline{u'v'})_y$ in this region) in Figure 7b is also consistent with this northward shift, since N_x is positive on the northern flank and negative on the southern flank (note N_x may include a rotational component, which is absent in Figure 7a). Although this behavior is for a single time, the structure is consistent with periods of drift over a longer time series (not shown). During periods when the jet is stationary, there is less correlation between the jet location and the structure of the eddy forcing. Figure 7 also shows that the zonal component of the mean flow extends nearly to the bottom, whereas the Reynolds stress terms are largely confined to the upper 1000 m. This feature is in agreement with the results in QG models, where upper layer Reynolds stresses are solely responsible for jet forcing, even when the jets have a strong barotropic component [Thompson and Young, 2007]. Figure 7c presents \bar{u} and Z temporally averaged over a two year period. The zonal component of the mean flow is smoothed considerably due to the jet drift and there is no evident pattern in the eddy forcing. The small magnitude of Z near 49°S is consistent with the dissipation of the coherent zonal jets seen in Figure 5a.

4.2. Box B

[34] Box B (180°W to 170°W and 55°S to 48°S) is found to the east of the Campbell Plateau. The steep ridge of the Plateau's southern boundary, found upstream of box B, is responsible for generating a strong topographically-steered boundary current (Figure 2b). As the steered current moves northward it deflects to the east around 51°S into a region of flat bathymetry. This produces a strong, steady eastward jet occurring at 50.5°S . This jet then retroflects, which allows a westward jet to develop to the south. A second weaker eastward jet appears between 53°S and 54°S (Figures 8a and 8b).

[35] Energy exchange in this region is dominated by a conversion from EKE to MKE near the northern jet core. The strong current emitted from the Campbell Plateau generates substantial EKE (Figure 2c), which is efficiently converted into a strong zonal mean flow. Again, there is a slight asymmetry in the zonally-averaged profile of \mathcal{R} , although the potential for drift is limited by the shallow topography to the north and the topographic constraint on the upstream position of the jet. Within the retrograde jet, \mathcal{R} takes negative values, although the time average is dominated by a period of high EKE in 1994.

[36] Again, in this region the Reynolds stresses are surface intensified, but the vertical structure is equivalent barotropic. Figure 9 shows zonally and temporally-averaged \mathcal{R} at three different levels. The strength of the mean flow forcing decays by more than an order of magnitude below 1000 m. Still, the depth averaged profile (Figure 9d) retains most of the structure of the upper layer dynamics. Thus box B presents an example of a jet that is localized by topography, but further downstream is sustained by eddy-mean flow interactions. It is interesting, then, to consider how the jet evolves further downstream (box C), where its position is no longer strongly influenced by topography.

4.3. Box C

[37] Figure 10a shows a time series of zonal mean kinetic energy ZMKE (red) and EKE (blue) averaged over the latitudes 45°S to 65°S at 160°W and at a depth of 250 m. The temporal variability has a low frequency component not associated with individual eddies. Furthermore, there is little evidence of a seasonal cycle since peaks in energy are not correlated with particular times of year. Figure 10a shows that in this region a number of ZMKE peaks are preceded by peaks in EKE. These events are indicated by the grey bars in Figure 10a and the dotted lines in Figure 10b. Figure 10b shows the time evolution of the zonal component of the

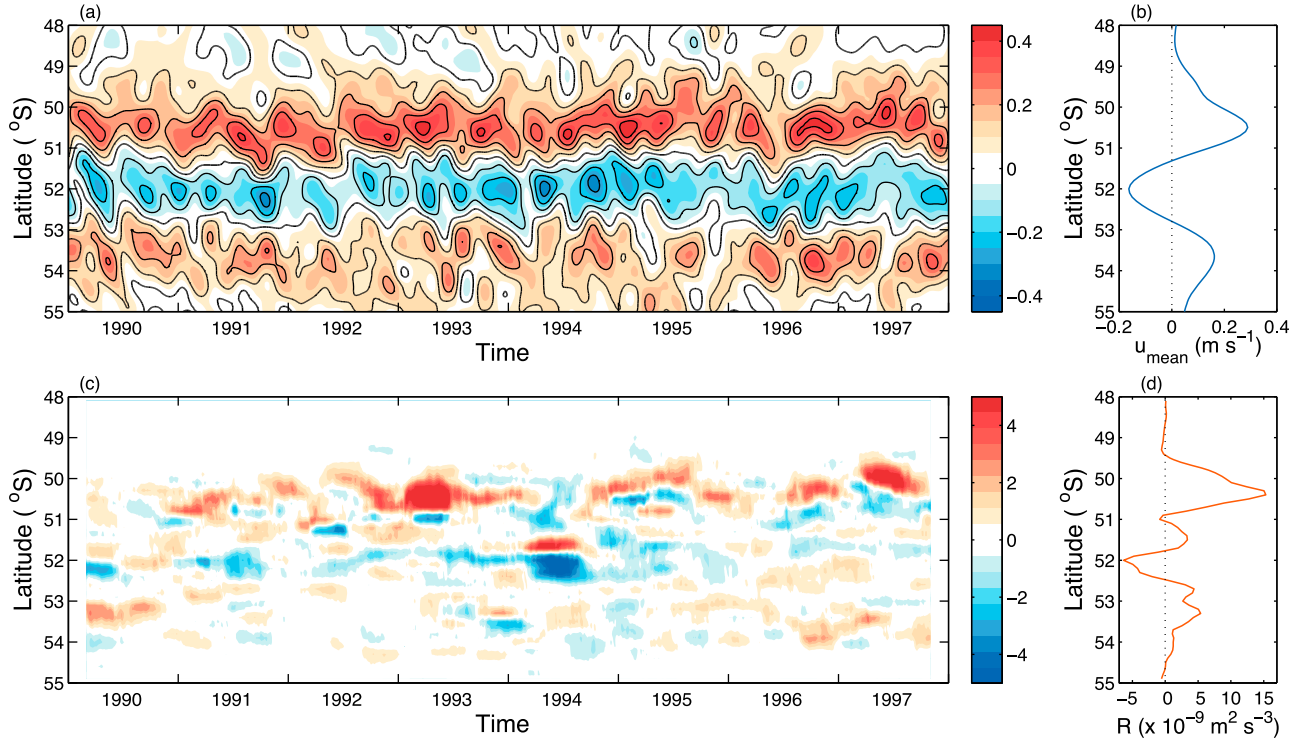


Figure 8. As in Figure 5, but for the domain indicated by box B (Figure 3): 180°W to 170°W and 55°S to 48°S.

mean velocity at 160°W. Jet behavior in this region, similar to many parts of the ACC, is characterized by a persistent eastward flow, although the magnitude and position of narrow coherent jets are time dependent. Four to five narrow jets can be found between 65°S and 50°S at all times. The

southern jets are generally weaker, but more persistent than their northern counterparts.

[38] The correlated peaks in EKE and ZMKE in Figure 10a can, in each of the three cases indicated by the gray bars, be linked to the appearance of strong, but transient, zonal jets

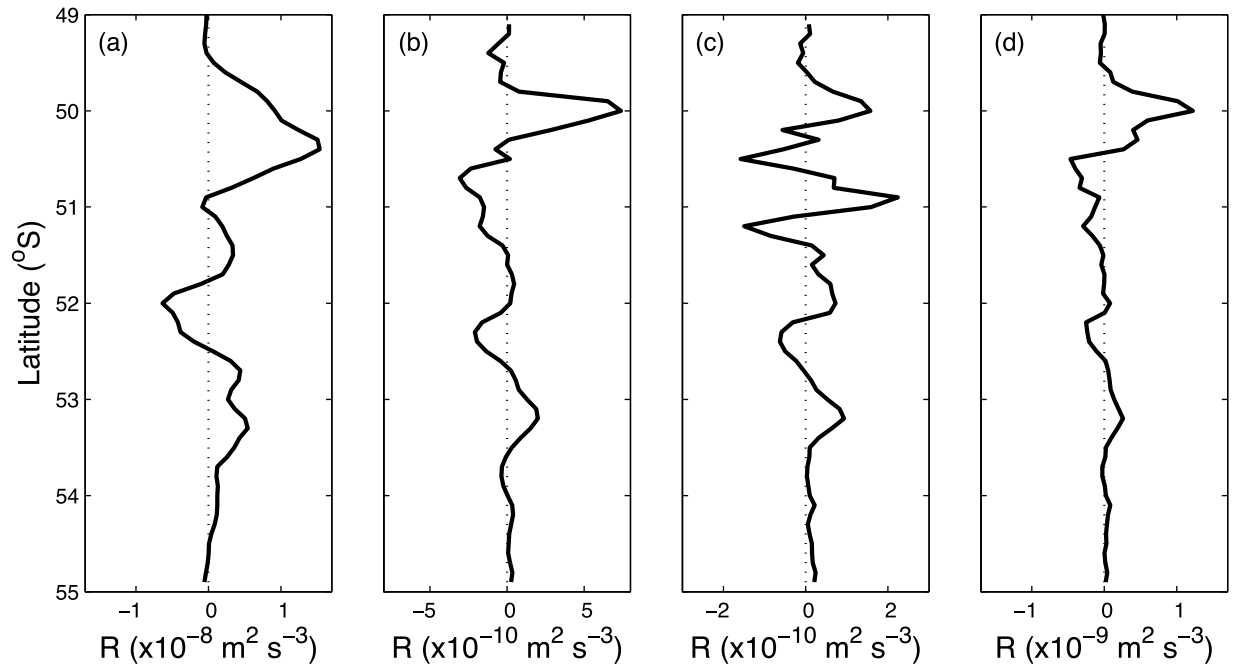


Figure 9. Time and zonal mean profile of R at (a) 250 m, (b) 1500 m and (c) 2500 m. (d) The depth averaged profile.

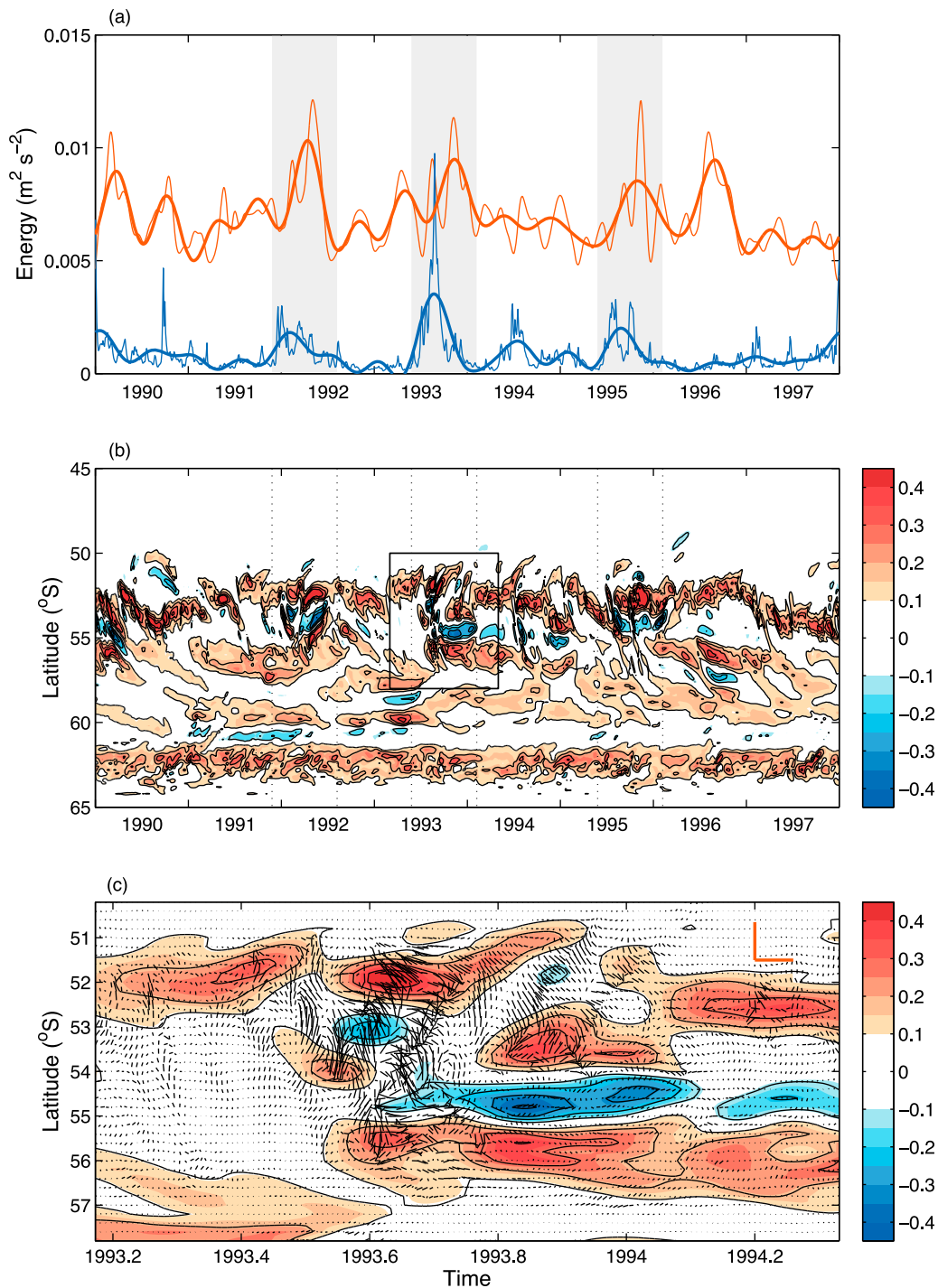


Figure 10. (a) Time series of zonal mean kinetic energy (ZMKE, red) and eddy kinetic energy (EKE, blue), as defined in section 3, averaged between 45°S and 65°S along 160°W . The bold curves show a further smoothing by taking a 60 day running mean in order to highlight the low frequency variability. The shaded bars indicate three times where peaks in EKE precede peaks in ZMKE. (b) Time-latitude plot of the zonal mean velocity along 160°W . The contours are every 0.1 m s^{-1} . The dotted lines indicate the extent of the shaded regions in Figure 10a. (c) Expanded view of the boxed region in Figure 10b. The arrows indicate eddy velocities, while the colors indicate the zonal mean velocity. The red arrows indicate 0.5 m s^{-1} velocities.

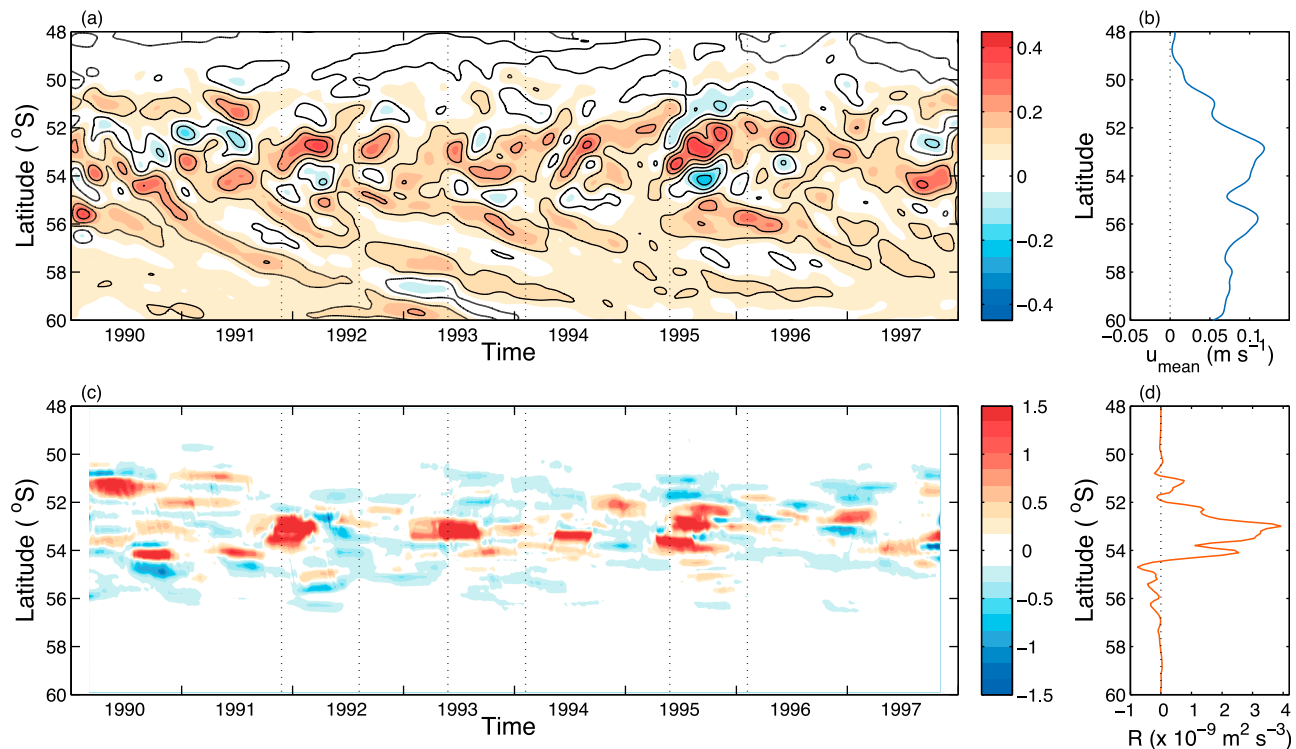


Figure 11. As in Figure 5, but for the domain indicated by box C (Figure 3): 165°W to 160°W and 60°S to 48°S.

between 53°S and 55°S. These occurrences are also notable because of the generation of a strong, but transient westward flow, indicative of divergence of eastward momentum outside of the jet cores [Vallis, 2006]. The appearance of these jets is typically preceded by a period of weak zonal flow near the formation region (especially in late 1991 and early 1993). An expanded view of the event in 1993 (Figure 10c) reveals that initiation of the strong zonal velocities (colors) is associated with a sharp enhancement of the eddy velocities (arrows). This burst of EKE is short-lived, lasting about two months, however jets that form as a result of this enhanced EKE persist for nearly a year. This rapid shift between states with high EKE and high ZMKE is reminiscent of the oscillating jet behavior described in section 2.2.

[39] It is reasonable to question whether the view taken along a single line of longitude, as in Figure 10, which offers a clearer dynamical interpretation, is representative of zonally-averaged properties in this region. Figure 11 shows time-latitude plots of zonally-averaged zonal component of the mean velocity (Figure 11a) and R over the longitude range 165°W to 160°W at 250 m depth (Figure 11c); their accompanying time averages appear in Figures 11b and 11d. Strong meandering of the flow in this region reduces the coherence of the zonal velocities, but the appearance of alternating eastward and westward flows in early 1992, late 1993 and mid 1995 are indicative of the jet formation events in Figure 10b. The time series of R in Figure 11c is dominated by three instances where R takes large positive values between 54°S and 52°S, indicating a transfer from EKE to MKE and the formation of strong zonal flows. All of the events occur at the onset of jet formation as described in Figure 10 (dotted lines).

4.4. Box D

[40] Box D (148°W to 133°W and 62°S to 50°S) presents another unique topographic regime due to the influence of the steep meridional Pacific-Antarctic Ridge (Figure 2a). Figure 12 shows the zonally averaged zonal component of the mean velocity (Figure 12, left) and R at 250 m depth with their accompanying time averages (profiles) (Figure 12, right). Box D is split into three sub-regions to focus on the transition in dynamics along the path of the ACC as it passes over the ridge.

[41] The flow in the first domain (box Di) is dominated by the ridge, which induces a strong steering of the mean flow (Figure 2b). A persistent zonal component to the flow is found at 56°S, although a clear poleward translation of coherent eddies is apparent between 54°S and 56°S. Figure 12b shows that this region north of 56°S is associated with $R < 0$, which would be consistent with the generation of EKE through baroclinic instability. On the southern flank of the jet there is a conversion to MKE. With respect to dynamics in the QG model, the asymmetry in the profile of R would suggest a southward drift. Here, though, the jet remains tied to the ridge's northern flank due to the steepness of the feature (cf. box A and box Di in Figure 3). Similar to box A, the positive Reynolds stresses are localized by topography on the northern slope of the ridge.

[42] In the second domain (box Dii), the dynamics of the eddy forcing have changed. The jet core remains at the same latitude, but the topography is now dominated by a sharp valley with a much shorter length scale than the broad ridge encountered in the first domain. As the width of the valley (≈ 20 km) is roughly the same size as the deformation radius,

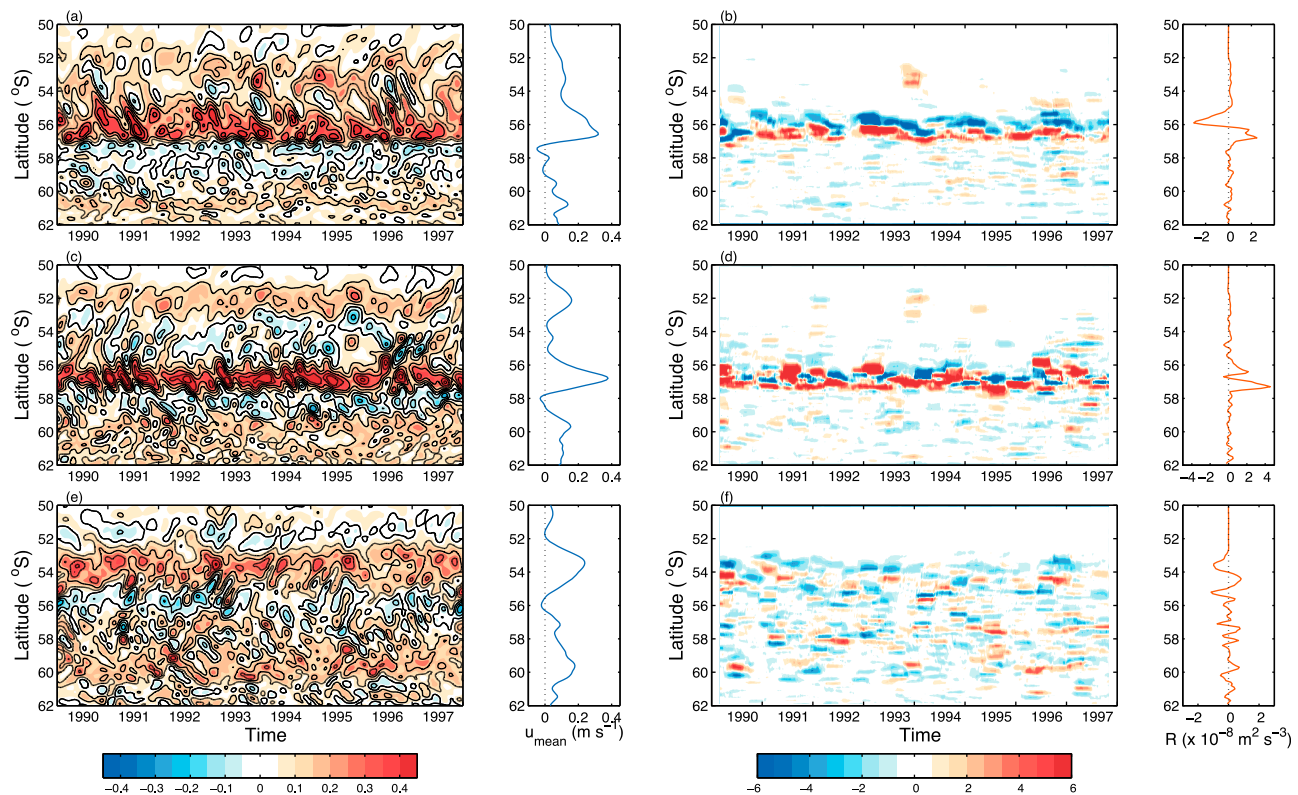


Figure 12. As in Figure 5, but for three subdomains in box D (Figure 3): (a,b) 148°W to 143°W, (c,d) 143°W to 138°W and (e,f) 138°W to 133°W. All domains span 62°S to 50°S in latitude.

it does not contribute strongly to the PV gradient felt by the jets (i.e. the topographic scale is smaller than the Rhines scale, ≈ 100 km). This leads to a transition to a regime where the jet forcing looks most similar to zonally-symmetric flows. The zonally-averaged profile of \mathcal{R} (Figure 12d) is weakly negative at the jet core, consistent with a transfer of energy from mean flow to EKE related to baroclinic instability, and roughly symmetric forcing of the zonal component of the mean flow on the flanks of the jet. This generates a persistent jet in this region (Figure 12c). Further downstream (box Diii) topography becomes important once more as a steep slope at 53.5°S constrains the position of a northern jet (Figure 12e). The displacement of this jet northward allows a second weaker jet to form near 60°S. In this final region the mean flow is topographically constrained, but does not have systematic enhancement or dissipation due to Reynolds stresses (Figure 12f).

5. Implications for Mixing

[43] Interest in jets derives from their ability to act as barriers to cross-jet transport [Rhines, 1994; Dritschel and McIntyre, 2008]. In this context jets typically act as boundaries between two relatively well-mixed regions, such that jet cores tend to be correlated with strong gradients in water mass properties. The relationship between velocity jets, as detected by sea surface height (SSH) gradients for instance, and subsurface water mass distributions is an area of active research. A thorough study by Langlais *et al.*

[2011] indicates that while jets can be accurately tracked using either SSH gradients or meridional temperature gradients, the positions of the jets in SSH space using the two methods are only weakly correlated. Figure 13 shows the relationship between the migrating jets in box A and the temperature distribution at the same depth.

[44] Figure 13a shows a time series of the zonally-averaged, meridional temperature gradient \bar{T}_y over box A (cf. Figure 5). The temperature gradient also undergoes a similar northward drift showing that the velocity jets are indeed tied to temperature fronts. Figure 13b shows the corresponding time series of zonally-averaged temperature. Regions where $\bar{T}_y > 0.01^\circ\text{C}/\text{km}$ are highlighted by the white contours. Inter-annual variations in the position of temperature contours are apparent, indicating that the jets are not moving through a fixed water mass structure. In Figure 13c we show a smoothed version of the temperature gradient time series from Figure 13a. An automated procedure picks out the local maxima in regions where the temperature gradient is continuously greater than $0.01^\circ\text{C}/\text{km}$ over a distance of approximately 70 km; the locations of these temperature gradient maxima are indicated by dots. Using these positions, the temperature at the core of each jet is tracked in Figure 13d. While the jets are not moving through a fixed water mass structure, neither are the temperature contours following the jets through a full five degrees of latitude. Instead, the southernmost jets form following periods when northward jet drift allows a uniform water mass to develop with a large meridional extent. This leads to alternating

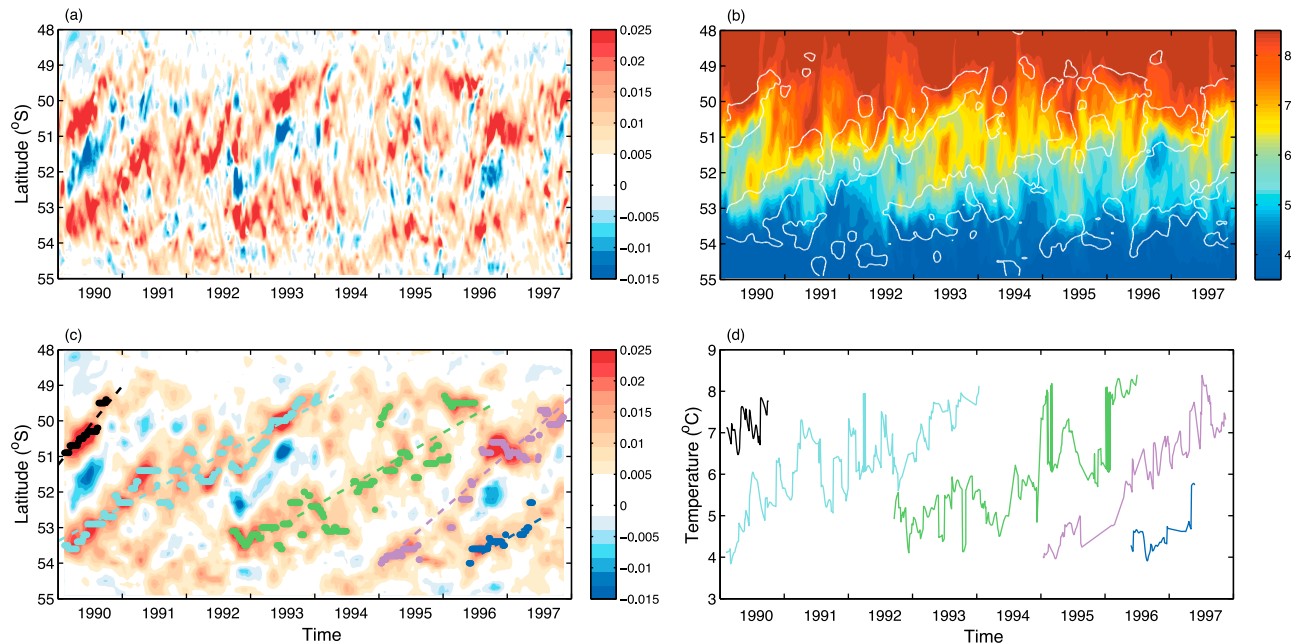


Figure 13. (a) Time-latitude plot of zonally averaged meridional temperature gradient (\overline{T}_y in $^{\circ}\text{C}/\text{km}$) in the region corresponding to box A (Figure 5). (b) Time-latitude plot of zonally averaged temperature ($^{\circ}\text{C}$). The white contour indicates regions where $\overline{T}_y > 0.01$. (c) Time series of \overline{T}_y using a running mean over a period $T_{\text{cut}} = 90$ days. The dots indicate positions of local maxima and the dashed lines are linear best fits to these points. Color are used to distinguish different drift events, but not necessarily a single jet. (d) Time series of temperature at the corresponding colored points in Figure 13c.

periods of single and multiple fronts and during the transition between these regimes, rapid shifts in temperature structure are apparent, e.g. late 1992/early 1993.

[45] Analysis of PV distributions in the Southern Ocean indicates that the efficiency of jets as barriers to transport varies spatially [Thompson *et al.*, 2010]. Marshall *et al.* [1993] and Sparling [2000] have shown that transport barriers can be diagnosed from histograms or probability density functions of materially conserved quantities. Crucially, histograms remove complications arising from spatial and temporal variations in the mean flow. Assuming a transport barrier separates two distinct water masses (or regions of PV), barriers appear as minima in the histograms of PV (number of grid points) separating maxima associated with the distinct water masses.

[46] Histograms also support the transition in dynamics between boxes B and C inferred from the Reynolds stress analysis. Figure 14 shows a time series of PV along the isopycnal $\sigma_2 = 36.75$, at the longitudes 176°W (Figure 14a), 170°W (Figure 14b), and 160°W (Figure 14c). In the western part of box B (Figure 14a), PV remains well mixed since the current ejected from the slope of the Campbell Plateau is a strong source of eddies, whose relative vorticity make a strong contribution to the PV. As the flow moves downstream, Reynolds stresses act to transfer this high EKE into the zonal flow and regions of distinct homogenized PV develop. At 170°E (Figure 14b) there is still a broad peak in PV spanning the range $q = 5 - 7 \times 10^{-11} [\text{ms}]^{-1}$. Further downstream (Figure 14c) the eddy activity is weaker and the PV distribution is more peaked, with sharper gradients

between the homogenized regions. The red curves, indicating the mean latitude of the PV values over the time series, also become more step-like as the flow progresses downstream, although there is considerably smoothing compared to the histograms. This transition has similarities to the cycle described in section 2.2, however here the cycle occurs along the path of the ACC, rather than locally over time.

[47] Finally, jet formation and dissipation cycles may also impact PV structure over time in local regions of the ACC. Figure 15 shows the time evolution of a histogram of PV on the $\sigma_2 = 36.75$ potential density surface corresponding to box C. Here color represents the number of grid points with a certain PV value over the region 60°S to 45°S and 159°W to 161°W ; this narrow longitude range (~ 60 km, still many times the first baroclinic deformation radius) is chosen for comparison with Figure 10. Two different states are apparent. At times the histogram is double-peaked, as during most of 1994 and 1997. At other times, though, the PV distribution has a single large peak such as in late 1991 and 1993. The transition from a double peak to a single peak in PV implies that a strong mixing event has occurred, likely associated with enhanced EKE levels. The white arrows in Figure 15 correspond to the gray bars in Figure 10, which highlight periods of enhanced EKE. Following these mixing periods the double-peaked PV structure is re-established, due to the emergence of strong zonal flows. This behavior is not related to an obvious seasonal signal as the three instances of the cycle (arrows) occur at different times during the year. However, this behavior may correlate with other modes of

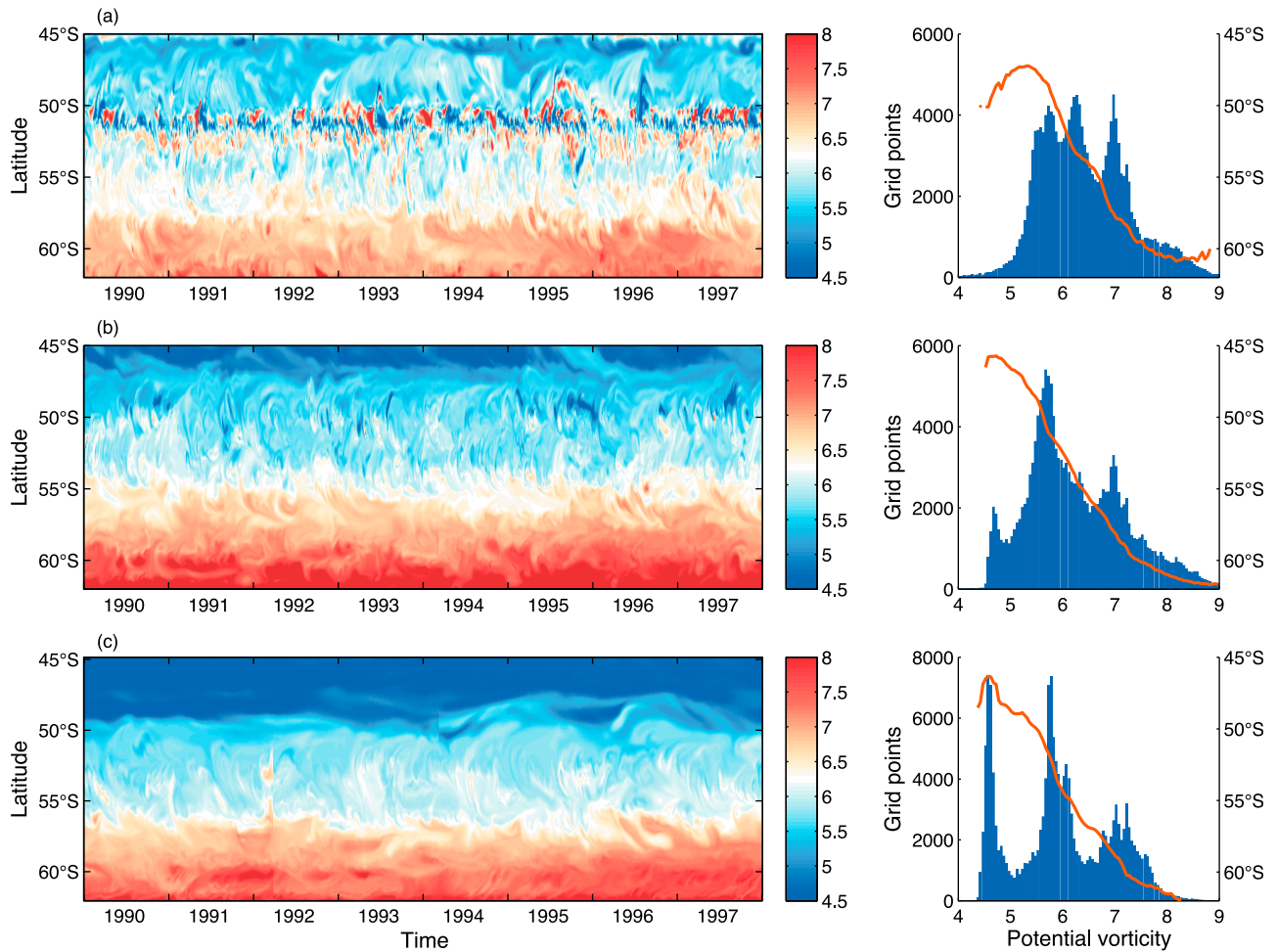


Figure 14. (left) Time-latitude plot of potential vorticity ($\times 10^{-11} [\text{ms}]^{-1}$) on the $\sigma_2 = 36.75 \text{ kg m}^{-3}$ isopycnal at (a) 176°E , (b) 170°E and (c) 160°E . (right) Histograms of the PV values found on the left. The red curves indicate the mean latitudes of PV over the time series on the left.

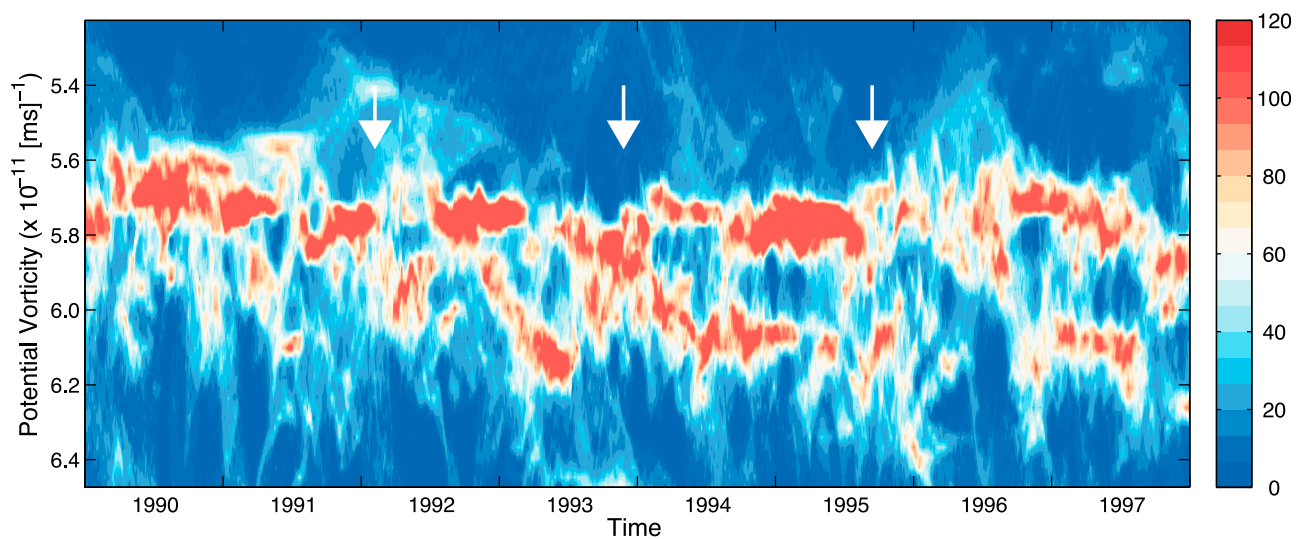


Figure 15. Time evolution of histograms of potential vorticity on the $\sigma_2 = 36.75 \text{ kg m}^{-3}$ isopycnal values between 60°S and 50°S and 159°W and 160°W . The color gives the number of grid points that fall within a PV bin; the PV discretization is $2.6 \times 10^{-13} [\text{ms}]^{-1}$. The three white arrows correspond to the positions of the gray bars in Figure 10a.

Southern Ocean or global variability, and would be an interesting topic to pursue.

6. Summary and Discussion

[48] This study has considered the low frequency variability of the ACC's fine-scale jets in an eddy-resolving ocean GCM. The study has revealed the richness in jet characteristics and dynamics. Three behaviors have been identified and analyzed: (i) drift in the meridional position of jet cores, (ii) the downstream evolution of jets and their efficiency as transport barriers following interaction with topography and (iii) intermittent formation and dissipation of transient jets. The jet behavior and dynamics exhibit many similarities to those seen in QG models [Hogg and Blundell, 2006; Thompson, 2010].

[49] Topography plays a key role in the distribution of EKE in the Southern Ocean [Aiki and Richards, 2008, and references therein]. Regions of high EKE in the ACC are generally sites of jet generation and in regions where EKE fluctuates significantly, jets preferentially form at times when EKE levels are high. Mean flows generated during these strong mixing states tend to persist over timescales that are longer than the period of the energy peak itself. Similarly, jets persist downstream of high EKE regions. Topography also helps determine the spatial structure of the Reynolds stresses. Although these realistic, primitive equation flows do not generate Reynolds stresses that are as regular as seen in QG models [Thompson, 2010], asymmetric forcing of the jet cores still gives rise to jet drift and jets tend to form or dissipate near transitions in the topographic slope. We note that mechanisms for migrating jets have also been observed in cases without topography, for example, Chan *et al.* [2007] describe a primitive equation, zonally symmetric channel that generates drifting jets due to a residual circulation that sets up an asymmetry in the baroclinicity about the jet core. Interestingly, the drift seen in box A has a similar sense to this study and indeed, with surface-intensified Reynolds stresses, the sense of the horizontal momentum flux shown in Figure 1 will move the baroclinic zone equatorward. Still, the tight adherence of the drift to the region spanned by the ridge suggests that interaction with topography is a dominant factor.

[50] The regions analyzed in this study indicate that jet characteristics vary significantly along the path of the ACC. Topographic localization can produce strong, persistent jets, whereas outside of these regions, it can be more difficult to attribute a unique signature to a jet. A specific case is the drifting jet in box A. Although there is evidence that jets are tied to specific sea surface height contours [Sokolov and Rintoul, 2007], a time-averaged view of this jet is unlikely to capture the dynamical transitions when, for instance, the temperature contours in Figure 13b rapidly shift to a more southern position. Thus although jets are observed everywhere within the ACC, care must be taken in the local application of global jet or front definitions. This study represents a step toward building a library of key dynamics that impact mixing and transport in the Southern Ocean, but work remains to be done in incorporating these physical processes into global theories of the Southern Ocean circulation.

[51] Section 5 suggests that these regional dynamics will indeed impact large-scale Southern Ocean properties since variability in transport properties, as suggested by the PV distributions, have implications for water mass modification. Recently Naveira-Garabato *et al.* [2011] have shown that Southern Ocean jets may act as either barriers to transport or be "leaky." Leaky jets are typically found near topographic features. The regions analyzed here indicate two instances in which jets may be leaky. The first is the situation where jets are largely induced by topography, and give rise to significant eddy generation. In this case the jet is not sustained by the eddy-mean flow interactions associated with idealized balanced models, although this scenario may become important downstream of the topographic feature (e.g. box B and box D). Here the topographically induced background mean flow may not be sufficient to limit transport across the jet path in the presence of strong meandering or eddies (Figure 14a). The second scenario involves the cyclic formation and dissipation of a jet that is preceded and followed by periods of intense mixing. Observations of mixing and mean flow strength that involve temporal averages may predict both strong mixing and strong zonal flows although both features are intermittent. This behavior is a difficult but important feature that needs to be parameterized in general circulation models unable to explicitly resolve eddies.

[52] In the work of Thompson [2010], unsteady jet behavior associated with bursts in mixing, were generated by topographic steering and modification of baroclinic instability characteristics. It is likely that there are a range of mechanisms that may modulate EKE levels in the real ACC, including non-local exchanges between mean and eddy energies. Indeed, Venaille *et al.* [2011] suggest that coherent eddies that form in unstable regions may be advected by the mean flow and impact flow characteristics further downstream. Accurately capturing these dynamics will be essential for predictions of the global circulation and climate. In particular, accounting for the spatial and temporal variation of tracer mixing caused by the multifaceted behavior of the jets poses a challenging task.

[53] **Acknowledgments.** The authors gratefully acknowledge the provision of OFES output by Hideharu Sasaki. We thank two reviewers for their comments, which significantly improved this manuscript. We also acknowledge helpful conversations with Chris Wilson. AFT was supported by a NERC postdoctoral fellowship, NE/E013171/1.

References

- Aiki, H., and K. J. Richards (2008), Energetics of the global ocean: The role of layer-thickness form drag, *J. Phys. Oceanogr.*, **38**, 1845–1869.
- Arbic, B. K., and G. R. Flierl (2004), Effects of mean flow direction on energy, isotropy and coherence of baroclinically unstable beta-plane geostrophic turbulence, *J. Phys. Oceanogr.*, **34**, 77–93.
- Belkin, I. M., and A. L. Gordon (1996), Southern Ocean fronts from the Greenwich meridian to Tasmania, *J. Geophys. Res.*, **101**, 3675–3696.
- Bower, A. S., H. T. Rossby, and J. L. Lillibridge (1985), The Gulf Stream—Barrier or blender?, *J. Phys. Oceanogr.*, **15**, 24–33.
- Chan, C. J., R. A. Plumb, and I. Cerovecki (2007), Annular modes in a multiple migrating zonal jet regime, *J. Atmos. Sci.*, **64**, 4053–4068.
- Dritschel, D. G., and M. E. McIntyre (2008), Multiple jets as PV staircases: The Phillips effect and the resilience of eddy-transport barriers, *J. Atmos. Sci.*, **65**, 855–874.
- Esler, J. G. (2008), Robust and leaky transport barriers in unstable baroclinic flows, *Phys. Fluids*, **20**, 116602, doi:10.1063/1.3013631.

- Ferrari, R., and M. Nikurashin (2010), Suppression of eddy mixing across jets in the Southern Ocean, *J. Phys. Oceanogr.*, **40**, 1501–1519.
- Gille, S. T. (1997), The Southern Ocean momentum balance: Evidence for topographic effects from numerical model output and altimeter data, *J. Phys. Oceanogr.*, **27**, 2219–2232.
- Hallberg, R., and A. Gnanadesikan (2006), The role of eddies in determining the structure and response of the wind-driven Southern Hemisphere overturning: Results from the modeling eddies in the Southern Ocean (MESO) project, *J. Phys. Oceanogr.*, **36**, 2232–2252.
- Hogg, A. McC., and J. R. Blundell (2006), Interdecadal variability of the Southern Ocean, *J. Phys. Oceanogr.*, **36**, 1626–1645.
- Hoskins, B. J., I. N. James, and G. H. White (1983), The shape, propagation and mean-flow interaction of large-scale weather systems, *J. Atmos. Sci.*, **40**, 1595–1612.
- Hughes, C. W., and E. R. Ash (2001), Eddy forcing of the mean flow in the Southern Ocean, *J. Geophys. Res.*, **106**, 2713–2722.
- Ivchenko, V. O., S. Danilov, and D. Olbers (2008), Eddies in numerical models of the Southern Ocean, in *Ocean Modeling in an Eddying Regime*, *Geophys. Monogr. Ser.*, vol. 177, edited by M. W. Hecht and H. Hasumi, pp. 177–198, AGU, Washington, D. C.
- Kamenkovich, I., P. Berloff, and J. Pedlosky (2009), Anisotropic material transport by eddies and eddy-driven currents in a model of the North Atlantic, *J. Phys. Oceanogr.*, **39**, 3162–3175.
- Langlais, C., S. Rintoul, and A. Schiller (2011), Variability and mesoscale activity of the Southern Ocean fronts: Identification of a circumpolar coordinate system, *Ocean Modell.*, **39**, 79–96.
- Lee, S. (1997), Maintenance of multiple jets in a baroclinic flow, *J. Atmos. Sci.*, **54**, 1726–1738.
- Lenn, Y.-D., T. K. Chereskin, J. Sprintall, and J. L. McClean (2011), Near-surface eddy heat and momentum fluxes in the Antarctic Circumpolar Current in Drake Passage, *J. Phys. Oceanogr.*, in press.
- Lu, J., and K. Speer (2010), Topography, jets and eddy mixing in the Southern Ocean, *J. Mar. Res.*, **68**, 479–502.
- Marshall, D. (1995), Topographic steering of the Antarctic Circumpolar Current, *J. Phys. Oceanogr.*, **25**, 1636–1650.
- Marshall, J., and T. Radko (2003), Residual-mean solutions for the Antarctic Circumpolar Current and its associated overturning circulation, *J. Phys. Oceanogr.*, **33**, 2341–2354.
- Marshall, J., D. Olbers, H. Ross, and D. Wolf-Gladrow (1993), Potential vorticity constraints on the dynamics and hydrography of the Southern Ocean, *J. Phys. Oceanogr.*, **23**, 465–487.
- Marshall, J., E. Shuckburgh, H. Jones, and C. Hill (2006), Estimates and implications of surface eddy diffusivity in the Southern Ocean derived from tracer transport, *J. Phys. Oceanogr.*, **36**, 1806–1821.
- Masumoto, Y., et al. (2004), A fifty-year eddy-resolving simulation of the World Ocean—Preliminary outcomes of OFES (OGCM for the Earth Simulator), *J. Earth Simul.*, **1**, 35–56.
- Mazloff, M. R., P. Heimbach, and C. Wunsch (2010), An eddy-permitting Southern Ocean state estimate, *J. Phys. Oceanogr.*, **40**, 880–899.
- McClean, J., S. Jayne, M. Maltrud, and D. Ivanova (2008), The fidelity of ocean models with explicit eddies, *Ocean Modeling in an Eddying Regime*, *Geophys. Monogr. Ser.*, vol. 177, edited by M. W. Hecht and H. Hasumi, pp. 149–163, AGU, Washington, D. C.
- McIntyre, M. E. (1970), On the non-separable baroclinic parallel flow instability problem, *J. Fluid Mech.*, **40**, 273–306.
- Munk, W. H., and E. Palmén (1951), Note on the dynamics of the Antarctic Circumpolar Current, *Tellus*, **3**, 53–55.
- Naveira-Garabato, A., R. Ferrari, and K. Polzin (2011), Eddy stirring in the Southern Ocean, *J. Geophys. Res.*, doi:10.1029/2010JC006818, in press.
- Olbers, D., D. Borowski, C. Völker, and J.-O. Wölff (2004), The dynamical balance, transport and circulation of the Antarctic Circumpolar Current, *Antarct. Sci.*, **16**, 439–470.
- Orsi, A. H., T. W. Whitworth III, and W. D. Nowlin Jr. (1995), On the meridional extent and fronts of the Antarctic Circumpolar Current, *Deep Sea Res.*, Part I, **42**, 641–673.
- Panetta, R. L. (1993), Zonal jets in wide baroclinically unstable regions: Persistence and scale selection, *J. Atmos. Sci.*, **50**, 2073–2106.
- Pedlosky, J. (1987), *Geophysical Fluid Dynamics*, Springer, New York.
- Rhines, P. B. (1994), Jets, *Chaos*, **4**, 313–339.
- Rintoul, S. R., C. W. Hughes, and D. Olbers (2001), The Antarctic Circumpolar Current system, in *Ocean Circulation and Climate*, edited by G. Siedler, J. Church, and J. Gould, pp. 271–302, Academic, London.
- Sinha, B., and K. J. Richards (1999), Jet structure and scaling in Southern Ocean models, *J. Phys. Oceanogr.*, **29**, 1143–1155.
- Spall, M. A. (2000), Generation of strong mesoscale eddies by weak ocean gyres, *J. Mar. Res.*, **58**, 97–116.
- Smith, K. S. (2007), Eddy amplitudes in baroclinic turbulence driven by nonzonal mean flow: Shear dispersion of potential vorticity, *J. Phys. Oceanogr.*, **37**, 1037–1050.
- Smith, W. H. F., and D. T. Sandwell (1997), Global sea floor topography from satellite altimetry and ship depth soundings, *Science*, **277**, 1956–1962.
- Sokolov, S., and S. R. Rintoul (2002), Structure of Southern Ocean fronts at 140°E, *J. Mar. Syst.*, **37**, 151–184.
- Sokolov, S., and S. R. Rintoul (2007), Multiple jets of the Antarctic Circumpolar Current south of Australia, *J. Phys. Oceanogr.*, **37**, 1394–1412.
- Sokolov, S., and S. R. Rintoul (2009), Circumpolar structure and distribution of the Antarctic Circumpolar Current fronts: 1. Mean circumpolar paths, *J. Geophys. Res.*, **114**, C11018, doi:10.1029/2008JC005108.
- Sparling, L. C. (2000), Statistical perspectives on stratospheric transport, *Rev. Geophys.*, **38**, 417–436.
- Thompson, A. F. (2008), The atmospheric ocean: Eddies and jets in the Antarctic Circumpolar Current, *Philos. Trans. R. Soc. A*, **366**, 4529–4541.
- Thompson, A. F. (2010), Jet formation and evolution in baroclinic turbulence with simple topography, *J. Phys. Oceanogr.*, **40**, 257–278.
- Thompson, A. F., and W. R. Young (2007), Two-layer baroclinic eddy heat fluxes: Zonal flows and energy balance, *J. Atmos. Sci.*, **64**, 3214–3231.
- Thompson, A. F., P. H. Haynes, C. Wilson, and K. J. Richards (2010), Rapid Southern Ocean front transitions in an eddy-resolving ocean GCM, *Geophys. Res. Lett.*, **37**, L23602, doi:10.1029/2010GL045386.
- Vallis, G. K. (2006), *Atmospheric and Oceanic Fluid Dynamics*, Cambridge Univ. Press, Cambridge, U. K.
- Venaille, A., et al. (2011), Baroclinic turbulence in the ocean: Analysis with primitive equation and quasi-geostrophic simulations, *J. Phys. Oceanogr.*, in press.
- Walker, A., and J. Pedlosky (2002), Instability of meridional baroclinic currents, *J. Phys. Oceanogr.*, **32**, 1075–1093.
- Williams, R. G., C. Wilson, and C. W. Hughes (2007), Ocean and atmosphere storm tracks: The role of eddy vorticity forcing, *J. Phys. Oceanogr.*, **37**, 2267–2289.
- Wilson, C., and R. G. Williams (2006), Where are eddy tracer fluxes directed downgradient?, *J. Phys. Oceanogr.*, **36**, 189–201.

K. J. Richards, International Pacific Research Center, School of Ocean and Earth Science and Technology, University of Hawaii at Manoa, Honolulu, HI 96822, USA.

A. F. Thompson, Division of Geological and Planetary Sciences, California Institute of Technology, Pasadena, CA 91125, USA. (andrewt@caltech.edu)